Applied Nanoscience (2020) 10:1489–1499
https://doi.org/10.1007/s13204-020-01356-4

ORIGINAL ARTICLE

The impact of antisite disorder on the physical properties of $La_2FeB''O_6$ (B″ = Fe, Ni and Co) double perovskites

Ebtesam E. Ateia[1,2] · Amira T. Mohamed[1] · Hassan Elshimy[3]

Received: 16 October 2019 / Accepted: 11 March 2020 / Published online: 30 March 2020
© King Abdulaziz City for Science and Technology 2020

Abstract
The synthesis, structural, morphological characterization, as well as the magnetic properties, of a double perovskite family $La_2FeB''O_6$, (B″ = Fe, Co, and Ni) were studied. The investigated samples were synthesized by a modified citrate auto combustion route. The crystal structure and microstructure were refined applying Rietveld profile refinements with the help of the Maud Program. The difference between the detected and simulated powder diffraction patterns is minimized using the reliability index parameter. The presence of nanometric crystallite was confirmed by X-ray diffraction (XRD) and field emission scanning electron microscopy (FESEM). The presence of multiple oxidation states of Fe, Co and Ni were confirmed by X-ray photoelectron spectroscopy (XPS). The maximum value of exchange bias was obtained for $La_2Fe_2O_6$, while La_2FeNiO_6 recorded the minimum value. In the investigated samples, the different natures of antiphase boundaries (APBs) cause the lack of magnetic saturation at relatively high magnetic fields. On the other side, the existence of various magnetic interactions with different magnetic antisite disorder (ASD) initiate the system to change to spin glass state.

Keywords Antisite disorder · Double perovskite · Magnetization · Nano crystallite size

Introduction

As a subclass of perovskite-type oxides ABO_3, the double perovskite-type oxide $A_2B'B''O_6$ has attracted more and more attention (Morrow et al. 2014). Numerous significant benefits to the physicochemical properties, stability, affecting activity and high efficiency in novel applications can be introduced through the double perovskite formation (Xu et al. 2019).

The double perovskite structure may be considered as the 3-dimensional arrangement of single perovskites, $AB'O_3$ and $AB''O_3$, placed in an alternative manner in space (Dhilip et al. 2019). In B-site ordered double perovskites, alternating octahedra of $B'O_6$ and $B''O_6$ are expected to act in a complementary fashion (Vasala and Karppinen 2015). Numerous double perovskite materials of the general formula $A_2B'B''O_6$ show high ferromagnetic T_c and significant low field magnetoresistance (Alarcón-Suesca et al. 2019; Li et al. 2014). In addition, they can be considered as an important source of spin-polarized electrons (Erten et al. 2011).

A major disadvantage of the double perovskite materials is the misallocation of the B′ and B′′ ions, which do not organize themselves in the ideal alternating structure. The physical properties of these materials are strongly related to the variation of antisite disorder (ASD) of the system (Asaka et al. 2007; Singh and Majumdar 2011; Navarro et al. 2001).

The structure of double perovskites can be classified into ordering or disordering types, in such a manner that the two different cations B′ and B′′, may remain disordered at the B site, or they can order, forming a so-called B-site ordered double-perovskite type (Pilania et al. 2016).

The significant factors which affect B-site cation arrangement are namely the size, electronic configuration and charge of B-site cations and also the A/B size ratio (Anderson et al. 1993). In some situations, it is observed that the order is not complete. Simply, when the charge difference between B′ and B″ is two or less, order–disorder effects are most often encountered.

✉ Amira T. Mohamed
atawfik@sci.cu.edu.eg

[1] Physics Department, Faculty of Science, Cairo University, Giza, Egypt

[2] Egypt Nanotechnology Center (EGNC), Cairo University, El-Sheikh Zayed 12588, Egypt

[3] Physics Department, Faculty of Science, Ain Shams University, Cairo, Egypt

From the structural point of view, the flexibility of the structure and the $B'O_6$ (or B'') octahedral tilting allows combining several *d* elements with lanthanide and actinide elements (Kimura et al. 1998). Equally important, the elucidation of the physical properties involves a deep knowledge of the crystal structure stability, electro-magnetic configuration and bonding effect between atoms.

The present study is concerned with inorganic double perovskites, $La_2Fe_2O_6$, La_2FeCoO_6 and La_2FeNiO_6, in which the A-site element is rare-earth ions (La) and the B-site elements are transition metal ions. A crucial part of the motivation for the following study is to elucidate the role of both the difference in charge between B′ and B'' cations and their types on the physical properties of the samples. The suitable candidate sample can be easily deduced, by differentiating between the studied materials.

Experimental

Perovskites $La_2FeB''O_6$ (B'' = Fe, Ni and Co) were synthesized using the citrate auto combustion technique (Ateia et al. 2020a; Almessiere et al. 2019; Ateia et al. 2019). The metal nitrates La $(NO_3)_3{\cdot}6H_2O$, Fe $(NO_3)_3{\cdot}9H_2O$, Co $(NO_3)_2{\cdot}6H_2O$, Ni $(NO_3)_2{\cdot}6H_2O$ and citric acid were used as starting materials. All the metal nitrates are supplied by ACROS with high purity (99.999%). The nitrates were weighed according to the compositions of the desired samples and dissolved in deionized water. Citric acid and metal nitrates were mixed together with a ratio (1:1) with constant stirring to form the citrate precursor mixture. Stirring, heating and drying were continued until the samples under investigation were prepared. The details of the preparation method are shown in Fig. 1.

X-ray diffraction patterns of the $La_2Fe_2O_6$, La_2FeCoO_6 and La_2FeNiO_6 nano ferrite samples were collected using X-ray powder diffraction pattern (XRD) with a diffractometer (X'Pert PRO PANalytical, Netherland). It was operated at 45 kV and High Score Plus software. The crystal structures and microstructures were refined applying Rietveld profile refinements (MAUD 2.55 program).

The morphology and nanostructure of the samples were studied by field emission scanning electron microscopy (FESEM) using SEM Model Quanta 250 FEG attached with EDAX unit (energy dispersive X-ray analyses). The chemical states of various elements in $La_2FeB''O_6$ nano-crystallites were studied with the help of X-ray photoelectron spectroscopy (XPS) collected on K-ALPHA (Themo Fisher Scientific, USA) with monochromatic X-ray Al K-alpha radiation. The magnetization (emu/g) was measured at room temperature (300 K) using a vibrating sample magnetometer (VSM) Model Lake Shore 7410.

Results and discussion

The prepared samples are formed in a single-phase orthorhombic structure with space group *Pbnm* (#62 orthorhombic) for $La_2Fe_2O_6$ and *Pnma* (#62-orthorhombic) for both La_2FeCoO_6 and La_2FeNiO_6 as illustrated in Fig. 2a–d. The obtained structure fully matches with diffraction files (01-074-2203), (00-044-0361) and (01-088-0638) for $La_2Fe_2O_6$, La_2FeCoO_6 and La_2FeNiO_6, respectively. The Rietveld refinement of X-ray diffraction patterns for the synthesized samples is presented in Fig. 2b. In each panel, solid squares represent the observed

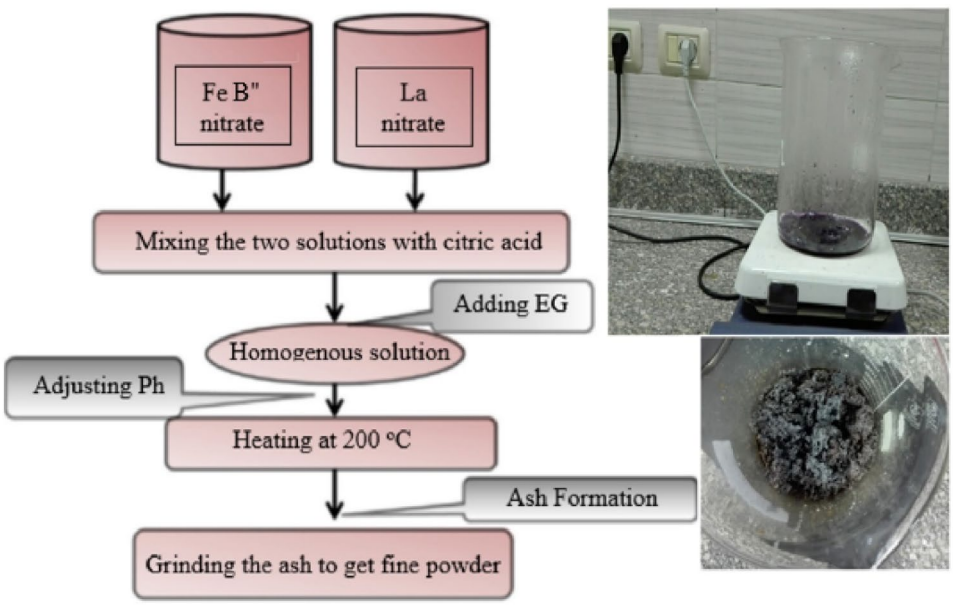

Fig. 1 Schematic flowchart for the preparation of double perovskite using modified citrate method

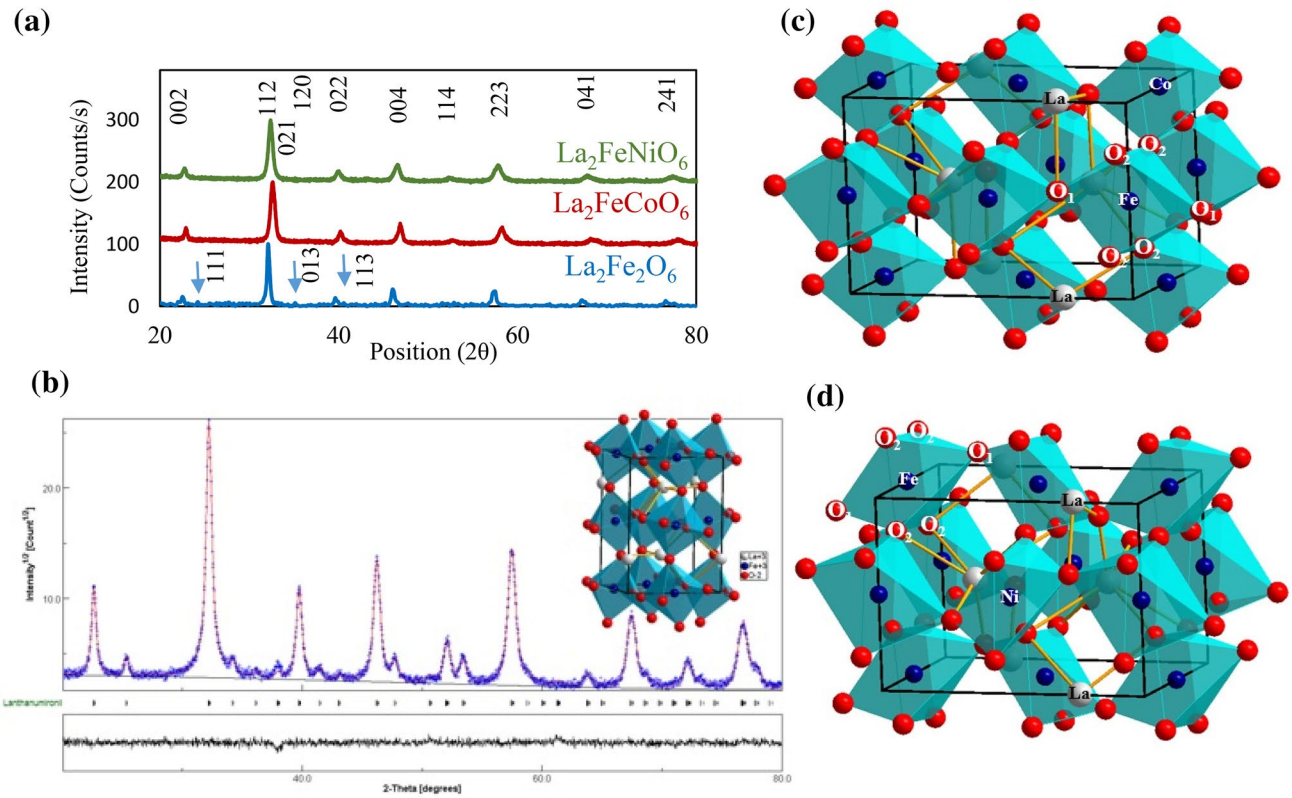

Fig. 2 Show **a** X-ray diffraction pattern of the prepared samples, **b** refinement profile for $La_2Fe_2O_6$ with the inset crystal structure, **c**, **d** crystal structure for La_2FeCoO_6 and La_2FeNiO_6, respectively

data; the line shows the calculated profile. The difference between the observed and the calculated pattern is shown at the bottom Rietveld refinement of the samples.

The difference between the detected and simulated powder diffraction patterns is minimized using the reliability index parameter, R_{wp} (weighted residual error), R_B (Bragg factor) and R_{exp} (expected error)(Abbas 2019; Fuster et al. 2015; Bhagwat et al. 2003). Consequently, the accuracy of the profile fitting is estimated by the following equations and the Rietveld parameters is tabulated in Table 1:

$$R_{wp} = \frac{\sum w_i (I_0 - I_c)^2}{\sum w_i I_0^2}^{1/2}, \tag{1}$$

$$R_{exp} = \left[\frac{N-P}{\sum w_i I_0^2}\right]^{1/2}, \tag{2}$$

$$R_b = \frac{\sum [I_0 - I_c]}{\sum I_0}, \tag{3}$$

$$\text{GOF} = \frac{R_w}{R_{exp}}, \tag{4}$$

where I_0 and I_c are the experimental and calculated intensities, respectively. Furthermore, $w_i(1/I_0)$ is the weight, N is the number of experimental observations and P is the number of fitting parameters. The refinement of the structural parameters is continued till convergence is optimized to a

Table 1 Values of lattice parameters, crystallite size and refinement parameters

Sample	Lattice parameter	Crystallite size (nm)	R_{exp}	R_{wp}	R_b	GOF
$La_2Fe_2O_6$	$a=5.540$, $b=5.558$ and $c=7.846$	19.000	18	20	14	1.1
$La_2Fe\ CoO_6$	$a=5.452$, $b=7.740$ and c=5.501	14.100	20	24	15	1.2
$La_2Fe\ NiO_6$	$a=5.544$, $b=7.768$ and $c=5.498$	12.959	19	17	11	0.9

goodness of fit (GOF) between 1.0 and 1.2 (Vandana and Rudramadevi 2017; Manik and Pradhan 2004; Lira-Hernández et al. 2016). The GOF values obtained in the present analysis suggests good refinements of the data.

It is important to note that the orthorhombic space group Pnma does not permit the ordering of the B-site cations over the six-coordinate sites of the perovskite structure (Tezuka et al. 2000; Ke et al. 2009). Thus, B-site ordering cannot be expected in La_2FeCoO_6 and La_2FeNiO_6, while in case of *Pbnm* it is quite different. Such order–disorder phenomena are of fundamental interest.

Considering the two classes of *hkl* reflections, the reflections with *hkl* all even are subcell reflections, and the *hkl* all odd reflections are superstructure reflections. In La_2FeCoO_6 and La_2FeNiO_6, the superstructure reflections disappear which indicate that there is no long-range order of the B cations, although the superstructure reflections are always broader than the subcell reflections so an expected order–disorder phenomenon are found. Besides, the most interesting order–disorder phenomena are found when the charge difference between the two cations equals "2", where a wide range of partial order may take place.

The average crystallite size is estimated using Scherer formula (Ateia and Mohamed 2017) and tabulated in Table 1. It confirms that the synthesized powder is polycrystalline, matching well in structure with previous reported data (Jin 2017).

The change of the lattice parameter is related to an increased octahedral tilting pattern of the perovskite framework. This occurs primarily for La_2FeCoO_6 and La_2FeNiO_6 due to decreasing the (M_B–O_1) and M_B–O_2 bond length, whereas bond length for $La_2Fe_2O_6$ remains unchanged (as shown in Table 2). In addition, B-site cation ordering has a remarkable influence on the electronic structure as well as lattice parameters which is mainly due to a large size mismatch between the Fe and Ni/Co ions.

However, the B′(B″) elements are balanced with transition metals with an O ion placed equally between each pair. If there is a difference between B′ and B″ in either charges or ionic radii the oxygen ions slightly change their position toward the more charged cation, while the octahedral symmetry of the $B'O_6$ and $B''O_6$ units is conserved.

Furthermore, two non-equivalent forms of oxygen (O_1, O_2) atoms are accompanied by the obtained structure. The two O_1 atoms are located on the *Z*-axis and four O_2 atoms are located on the *XY*-plane, as shown in Fig. 2c, d. On the other side, the structures with non-equivalent types of O atoms, where the angle B′–O_1–B″ remains unchanged (180°). While a little change of B′–O_2–B″ angle will take place. Table 2 illustrates the variation of bond lengths and bond angles according to the Rietveld refinements. During structural optimization, the *c*/*a* ratio is very close to the value of $\sqrt{2}$. This structure leads to the antiferromagnetic property, as will be discussed later in the magnetic measurements.

It is crucial to calculate the tolerance factor from Goldschmidt relation as follows (Markandeya et al. 2015):

$$t = \frac{r_A + r_o}{\sqrt{2} \times \left(\frac{r_{B'} + r_{B''}}{2} + r_o \right)}, \tag{5}$$

where r_A, $r_{B'}$, $r_{B''}$, r_o are the ionic radii of A, B′, B″ cations and oxygen ions, respectively. It can be detected that $LaFeB''O_6$ (B″ = Fe, Co and Ni) double perovskite presents a tolerance factor in the range of 0.9, 0.87 and 0.86 respectively, which are in a good agreement with the data obtained by Gorodea (2014). The structural "mismatch" gives rise to the rotation of $B'O_6$/$B''O_6$ polyhedra causing the movement of La cations while lowering symmetries and causing distorted perovskite structures.

Figure 3a–c shows field emission scanning electron microscopy images (FESEM) for $La_2Fe_2O_6$, La_2FeCoO_6 and La_2FeNiO_6, respectively. An irregularly conglomerated of small grain sizes is observed for all the investigated samples. However, the greater particle sizes are formed by smaller particles agglomerated. This observation agrees well with the crystallite size estimated from XRD data. The obtained data show that La_2FeNiO_6 sample has the lowest particle sizes which are corresponding to high agglomerations.

EDAX mapping of the samples is presented in Fig. 4a–c which indicates a homogeneous distribution of all the cations. The EDAX mapping images of La, Fe, Co, Ni and O are indicated by different colors, as shown in the figure. Although it is difficult to precisely analyze distribution of these elements, the mapping provides the notion that the elements are well distributed throughout the sample matrix.

During the sintering process, loss of ingredients may occur which leads to non-stoichiometry in the prepared samples. This, in turn, shows unexpected behavior. Consequently, it is essential to check the chemical stoichiometry of each sample. A representative energy dispersive analysis of X-rays (EDAX) pattern is shown in Fig. 5a–c. The semi-quantitative chemical composition analysis performed

Table 2 Refined values of bond lengths and bond angles obtained from Rietveld refinements

Samples	M_A–O_1	M_A–O_2	M_B–O_1	M_B–O_2	M_A–M_A	M_A–M_B	M_B–M_B	M_B–O_1–M_B	M_B–O_2–M_B
$La_2Fe_2O_6$	2.42	2.42	1.94	1.94	3.92	3.28	3.92	159	155
$La_2Fe\ CoO_6$	2.05	2.67	2.16	1.69	3.88	3.32	3.88	164	159
$La_2Fe\ NiO_6$	2.50	2.48	1.95	1.78	3.87	3.28	3.87	172	176

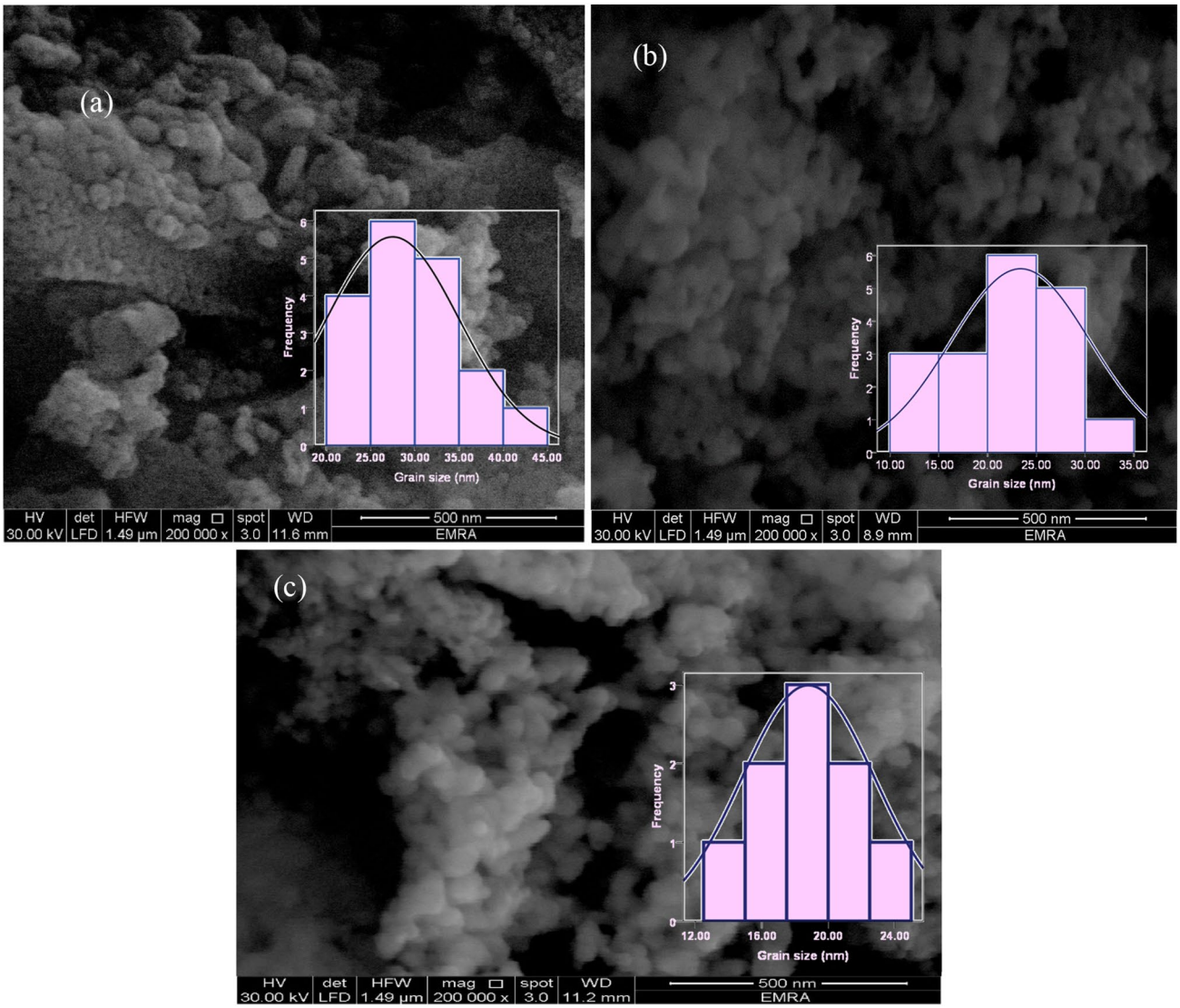

Fig. 3 Shows FESEM images for **a** $La_2Fe_2O_6$, **b** La_2FeCoO_6 and **c** La_2FeNiO_6. The inset histogram represents the grain size distribution

by EDAX suggests values that can be approximated to the empirical formula and confirm the stoichiometry. Differences in the values are attributed to little scattering X-ray diffraction of the oxygen. No trace of any impurity was found indicating the purity of the samples.

The chemical states of various elements in the samples is characterized by X-ray photoelectron spectra (XPS) technique. All XPS spectral peaks are fitted with CASAXPS software. The data analysis involved spectra normalization and Shirley background subtraction.

Figure 6a–e shows X-ray photoelectron spectra for $La_2Fe_2O_6$, $LaFeCoO_6$ and La_2FeNiO_6 samples. The Fe 2p spectrum consists of Fe $2p_{3/2}$ and Fe $2p_{1/2}$ excitations, as shown in Fig. 6a. The Fe $2p_{3/2}$ XPS signal can be divided into two peaks, one at (710.97, 710.29 and 709.77 eV) And thee other peak appears at (714.51, 713.01, and 712.89 eV) for $La_2Fe_2O_6$, $LaFeCoO_6$ and La_2FeNiO_6, respectively. The observed peaks are assigned to Fe^{3+} and Fe^{4+} (Rajagopalan and Chen 2017).

Similarly, the Fe $2p_{1/2}$ is divided into two peaks indicating the mixed oxidation state Fe^{3+}/Fe^{4+} (Ghaffari et al. 2012).

Moreover, the observed peaks at 719.14, 719.43 and 721.07 eV for $La_2Fe_2O_6$, $LaFeCoO_6$ and La_2FeNiO_6, respectively, are reported as Fe $2p_{3/2}$ satellite peaks as per NIST XPS database. These peaks confirm the presence of 3 + oxidation state of Fe. The feature peaks which are identified in La_2FeCoO_6 and La_2FeNiO_6 at 716.13 and 716.97, respectively, are corresponding to the presence of Fe^{2+} cation (Aguilar et al. 2019).

The relative percentages of Fe^{3+}/ Fe^{4+}in surface of $La_2Fe_2O_6$ are (0.72/0.28), while $Fe^{3+}/Fe^{4+}/Fe^{2+}$ in

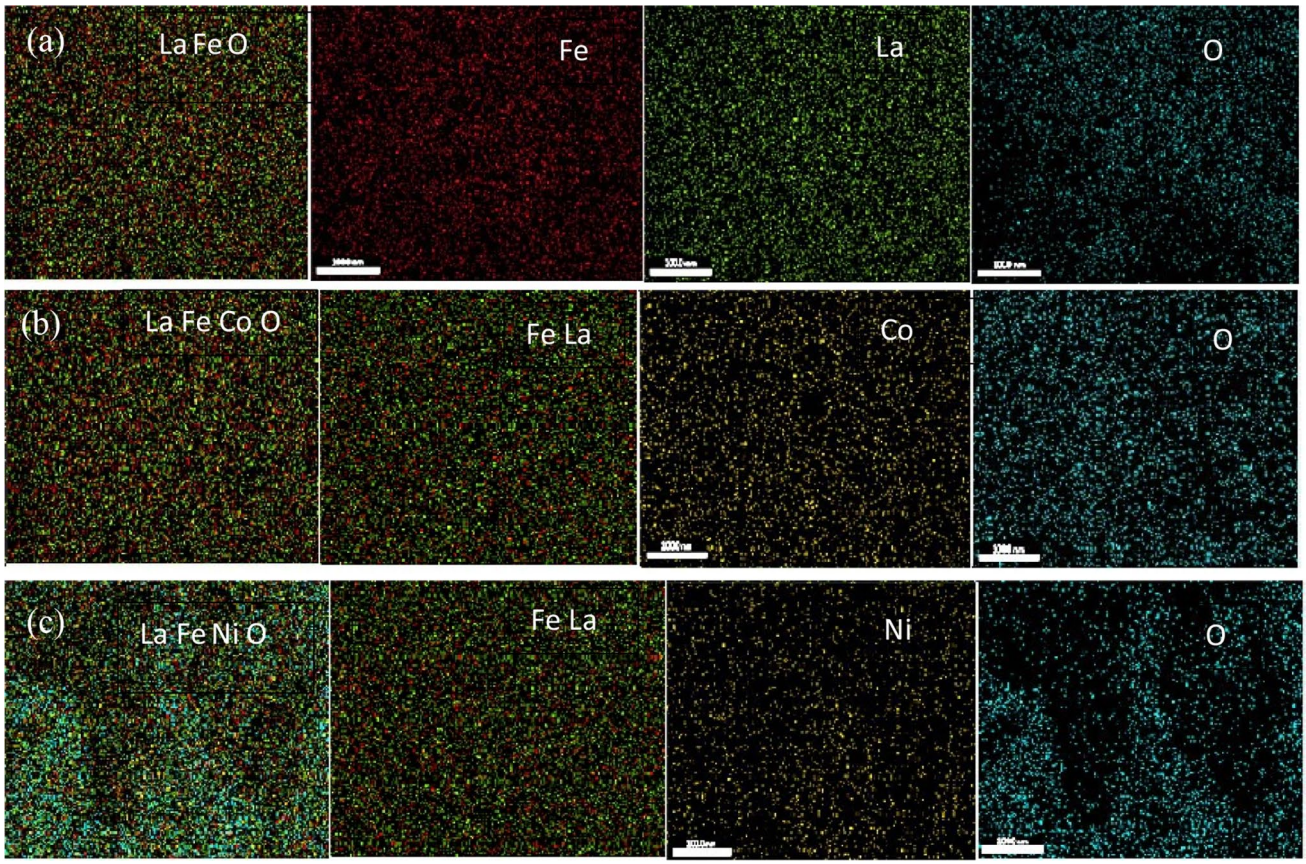

Fig. 4 **a–c** Represents the mapping images for $La_2Fe_2O_6$, and La_2FeCoO_6 and La_2FeNiO_6 respectively

La_2FeCoO_6 and La_2FeNiO_6 are (0.64/0.23/0.13) and (0.58/0.30/0.12), respectively.

Deconvolution of Co (2p) core level spectrum is shown in Fig. 6b. The $2P_{3/2}$ and $2P_{1/2}$ main characteristic peaks having a binding energy of 780.05 eV and 795.15 eV, respectively, are assigned to mixed Co^{3+}/Co^{2+} state (Singh and Kumar 2019; Sudha et al. 2019). Moreover, the weak satellite peak at 789.37 eV is assigned to CoO. Therefore, this analysis confirms the presence of Co^{2+} as well as Co^{3+} species (Silva et al. 2018). The relative percentage of Co^{3+}/Co^{2+} is (0.85/0.15).

The Ni 2p spectrum (Fig. 6c) consists of two spin–orbit doublets characteristic of Ni^{2+} and Ni^{3+} (Joshi et al. 2015). Clearly, additional feature develops at the low binding energy side (EB = 852.2 eV) which can be attributed to metallic Ni (Uhlenbrockt et al. 1992). The relative percentage of $Ni^{3+}/Ni^{2+}/No^{0}$ is (0.43/0.28/0.29).

The O 1s region is divided into three components in all prepared samples, as shown in Fig. 6e. According to Zhao et al. (2016), there are two kinds of oxygen in the double perovskite-type oxide. One is the adsorbed oxygen (O_2^{2-}, O_2^{1-}) with binding energy higher than 530.0 eV which is interrelated to the concentration of oxygen vacancies. Another is the lattice oxygen with binding energy lower than 530.0 eV. The ratio of O_{ads} (adsorbed oxygen) to O_{lat} (lattice oxygen) on the surface of each sample is in the order of $La_2Fe_2O_6$ (0.29) < La_2FeCoO_6 (0.65) < La_2FeNiO_6 (1.15).

According to the obtained data, La_2FeNiO_6 has a higher lattice defect compared to the other samples. This can be attributed to its lowest crystallite size and highest surface area.

The XPS spectrum for La is shown in Fig. 6d, where La 3d spectrum has two spin–orbit components of La $3d_{3/2}$ and La $3d_{5/2}$ with peaks appearing at binding energy nearly equal 838 and 833 eV, respectively, confirming La^{3+} oxidation state (Singh and Kumar 2019; Tulliani et al. 2013). The shakeup peak (shake-up satellites) with a binding energy of ≈ 851.5 eV may be due to the electron transfer from La atoms to the empty 4f subshell in the ionization process, as mentioned in the literature (Jørgensen and Berthou 1972). Besides, the low tolerance value obtained for La_2FeCoO_6 and La_2FeNiO_6 assures the oxygen defect in the samples.

Figure 7a–d represents the magnetic hysteresis loops for double perovskite samples with general formula $La_2Fe_2O_6$, La_2FeCoO_6 and La_2FeNiO_6. Magnetic hysteresis plots with different shapes suggest the existence of more than one

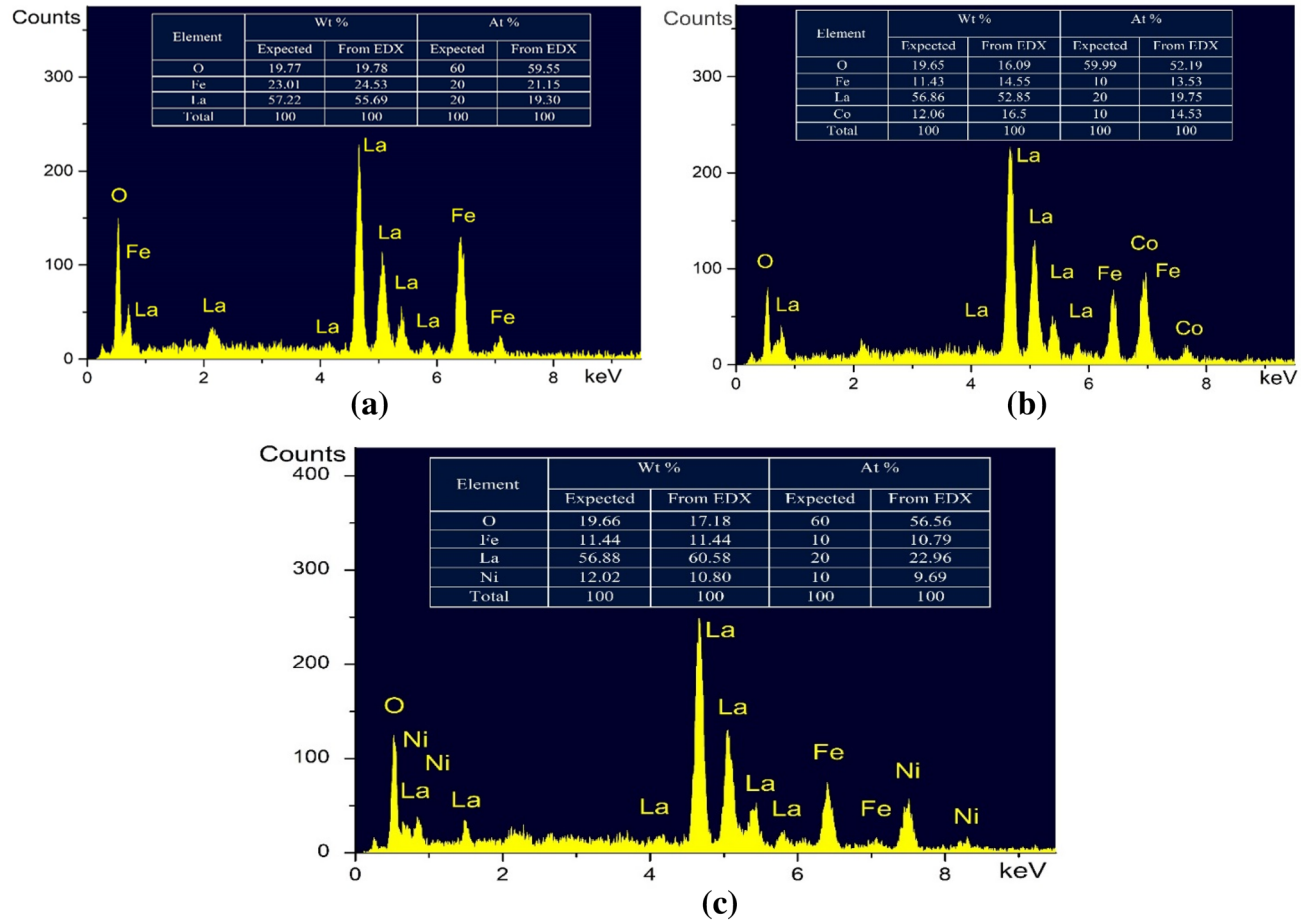

Fig. 5 Represent the EDAX spectra for **a** $La_2Fe_2O_6$, **b** La_2FeCOO_6 and **c** $LaFeNiO_6$

phase or an intrinsic inhomogeneity in the system. The magnetic parameters obtained from hysteresis loops such as the saturation magnetization (M_s), remanent magnetization (M_r), coercivity (H_c), hysteresis loss, exchange bias (H_{EB}) and squareness ratio are presented in Table 3.

As shown in the figure, the saturated fields are much different for the samples, which suggest that the antiferromagnetic coupling intensity in La_2FeCoO_6 and La_2FeNiO_6 samples are stronger than that in $La_2Fe_2O_6$ sample. This remarkable increase of antiferromagnetic coupling should be attributed to the formation of the antiferromagnetic antiphase boundaries (APBs) in the La_2FeNiO_6 and La_2FeCoO_6 samples the amount of APBs in La_2FeNiO_6 sample would be much larger than that in La_2FeCoO_6 sample.

The squareness ratio M_r/M_s determines the type of intergrain exchanges. In the case study, the squareness value is less than 0.5 (Table 3). Consequently, nanoparticles interact magnetostatically (Ateia et al. 2020b).

The small values of the coercivities for the investigated samples confirm the presence of competing ferri and antiferromagnetic interactions, which will be discussed later. On the other side, in the $La_2Fe_2O_6$ sample, the antisite disorders distribute separately in each $La_2Fe_2O_6$ grain, and there is no strong magnetic coupling among the antisite disorders. Thus, there are some ferromagnetic and antiferromagnetic moments in the investigated samples with high antisite disorder degree.

Exchange bias (H_{EB}) can be determined from the following equation (Mumtaz et al. 2007):

$$H_{EB} = -\left(H^{+} + H^{-}\right)/2, \tag{6}$$

where H^- and H^+ are the left and right coercivities. The obtained H_{EB} field for different B″ cations is tabulated in Table 3. The $La_2Fe_2O_6$ sample has a maximum value of 1.062 emu/g and 40 Oe, corresponding to saturation magnetization and exchange bias, respectively, while La_2FeNiO_6 sample records the minimum value, as shown in the Table. Therefore, by changing B″ type, one can effectively modulate the EB effect in the investigated samples.

Generally, the large number of probable combinations of B′, B″ in double perovskites produce a variety of magnetic

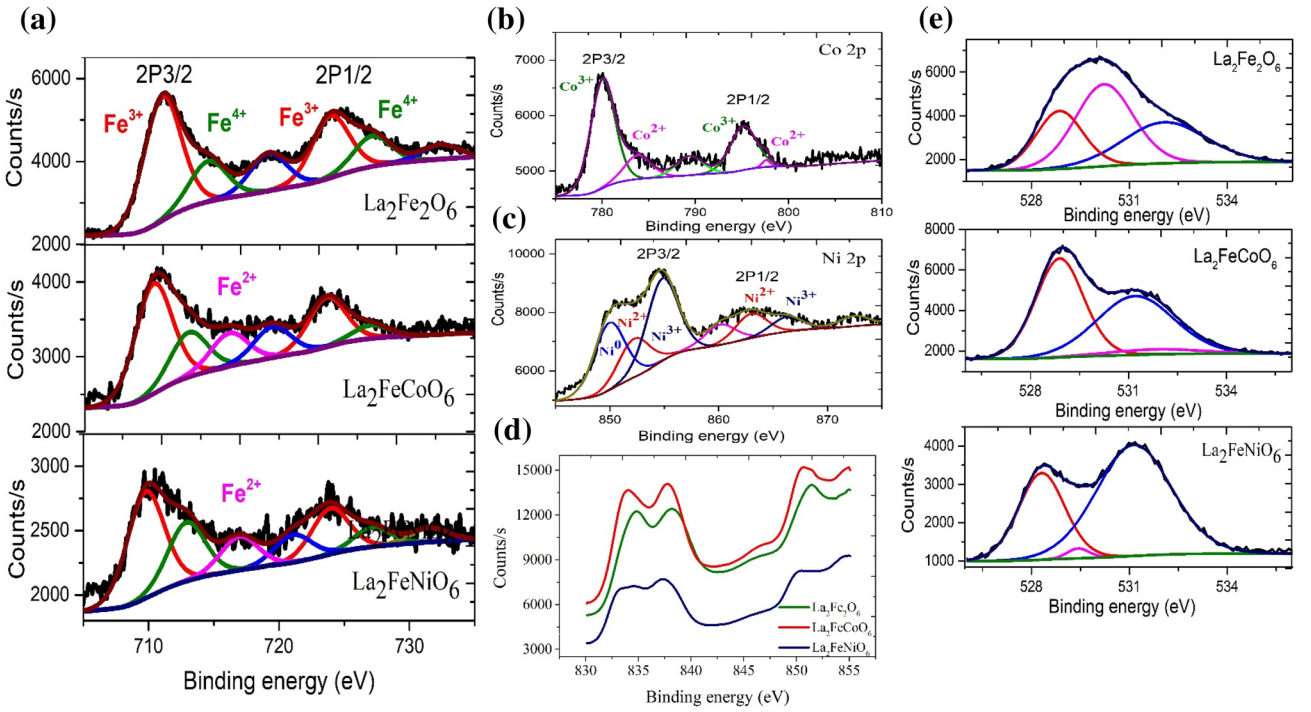

Fig. 6 X-Ray photoelectron spectroscopy (XPS) spectra of **a** Fe 2p, **b** Co 2p, **c** Ni 2p peak, **d** La 3d peak, and **e** oxygen for $La_2Fe_2O_6$, $LaFeCoO_6$ and La_2FeNiO_6 samples

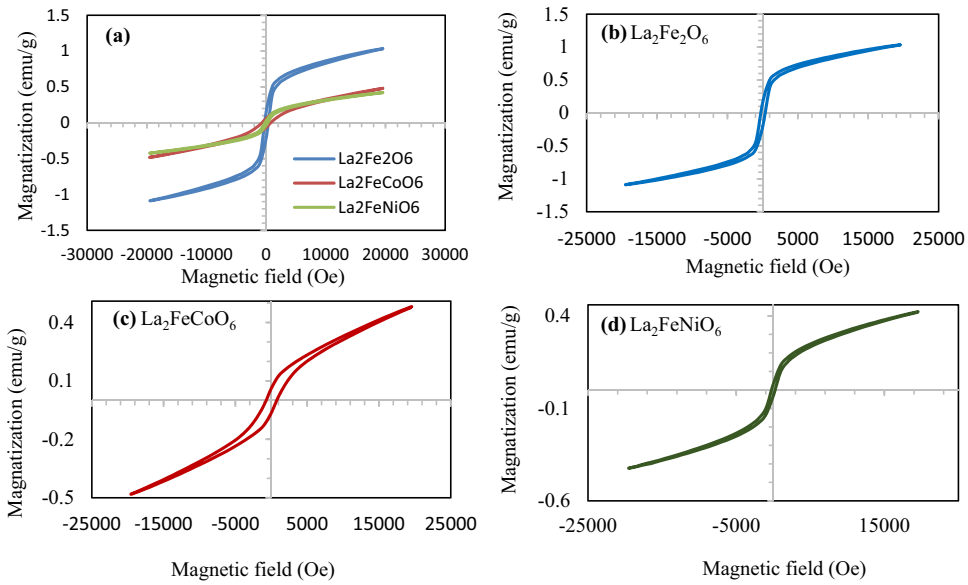

Fig. 7 **a**–**d** Represents the VSM hysteresis loops for the prepared samples

Table 3 Magnetic values of saturation magnetization (M_s), remanent magnetization (M_r), coercivity (H_c), hysteresis loss, exchange bias (H_{EB}) and squareness ratio (M_r/M_s)

Sample	M_s (emu/g)	M_r (emu/g)	H_c (Oe)	Energy loss (erg/g)	M_r/M_s	H_{EB} (Oe)	n_B (exp)
$La_2Fe_2O_6$	1.062	0.182	305	2018	0.171	40	0.092
La_2FeCoO_6	0.482	0.063	746	1121	0.130	15	0.042
La_2FeNiO_6	0.423	0.032	242	519	0.075	5	0.037

phases. These phases are ferromagnets, antiferromagnets and spin glass. Moreover, in case of study, there is deviation of bond angle (Fe–O–Ni), (Fe–O–Fe) and (Fe–O–Co) from 180° to 176°, 155°, 159°, respectively, as shown in Table 2 The bond-angle distortion decreases the effective d-electron hopping energy through the decreased hybridization between Ni, Fe, Co in "d" state and oxygen "p" states, leading to the insulating phase in the samples (Sclauzero et al. 2016). Antisite defects and antiphase boundaries are the most common way in which disorder at either A- or B-site cation sub-lattices can take place in double perovskites (Vasala and Karppinen 2015).

In the investigated samples, a crucial issue that influences their physical properties is antisite disorders (ASDs) (Navarro et al. 2001). The interchanging the ionic positions of B′ and B″ in the ordered structure (Morrow et al. 2014) is the main reason for the occurrence the antisite disorders (ASDs) in the samples, as shown in Fig. 8

Moreover, the ferromagnetic region consisting of Fe^{3+}–O^{2-}–$Co^{2+}$is separated by antiphase boundaries (APBs) resulting from antiferromagnetic super exchange interaction between Co^{2+}–O^{2-}–Co^{2+} and Fe^{3+}–O^{2-}–Fe^{3+}. The different natures of APBs cause the lack of magnetic saturation at relatively high magnetic fields (as shown in Fig. 7) (Krishna Murthy et al. 2017). On the other side, the existence of various magnetic interactions with different magnetic antisite disorder (ASD) initiate the system to change to spin glass state (Sahoo et al. 2017; Harbi et al. 2019). In other words, a large B-site disorder in the La_2FeCoO_6 can be attributed to the mismatching between the ionic radii of Fe (0.585 Å) and Co (0.745 Å) and the mixed-valence states of Fe^{3+}/Fe^{4+} /$Fe^{2+}$and Co^{2+}/Co^{3+}. This haphazard distribution leads to a competition between nearest neighbor and successive nearest neighbor superexchange interactions strengthening the local magnetic frustration in the lattice; consequently, the spin-glass phase appears in the sample.

On the other side, the changes in the ratio of Fe^{3+} ($3d^5$, S = 5/2) /Fe^{4+} ($3d^4$, S = 1)/Fe^{2+} ($3d^6$,S = 2) or Co^{2+} ($3d^7$, S = 3/2) /Co^{3+}($3d^6$, S = 2) for La_2FeCoO_6 samples leads to the change of magnetic moment, as shown in the table. Simultaneously, the presence of Fe^{4+} and Co^{3+}ions will weaken the FM interaction by creating other AFM pairs in the form of Co^{2+}–O^2–Co^{2+}, Co^{3+}–O^{2-}–Co^{3+}, Fe^{3+}–O^{2-}–Fe^{3+}, Fe^{4+}–O^2–Fe^{4+} etc. along with the FM coupling, such as Co^{2+}–O^{2-}–Fe^{4+} and Co^{3+}–O^{2-}–Fe^{3+} etc.

The Goodenough–Kanamori (GK) rules (Morrow et al. 2014; Ahmed et al. 2017) shows that a 180° superexchange coupling of two magnetic ions with partially filled d-shells can be strongly antiferromagnetic. In case study, the partially substituted La_2FeNiO_6 samples are showing antiferromagnetic properties due to the NiO_6 and FeO_6 octahedra gives rise to bond angle in the range of 176 °C of superexchange interactions between Ni^{2+} (d^8: t_{2g}^6 e_g^2)/Ni^{3+} (d^7: t_{2g}^6 e_g^1) and Fe^{3+} (d^5:$t_{2g}^5e_g^0$) according to Kanamori–Goodenough rule.

The small values of the coercivities for the investigated samples confirm the presence of competing ferri and antiferromagnetic interactions.

Interestingly, $LaFO_3$ possess AFM with canted Fe^{3+} spins as reported in the previous work (Ateia et al. 2017). This property changes to a ferrimagnetic in double perovskite $La_2Fe_2O_6$ sample. The change of valence state of Fe^{3+} in $LaFeO_3$ to mixed-valence states of Fe^{3+}/Fe^{4+} in $La_2Fe_2O_6$ is the main cause for the observed change. The Fe^{4+}–Fe^{3+} coupling is more stable than the Fe^{3+}–Fe^{3+} coupling, which is consistent with the XPS results as mentioned before.

Conclusion

The double Perovskites $La_2FeB''O_6$ (B'' = Fe, Ni and Co) were synthesized successfully using the modified citrate auto combustion technique. The crystal structure and microstructure were refined applying Rietveld profile refinements with the help of the Maud Program. The presence of nanometric crystallite was confirmed by X-ray diffraction (XRD) and Field Emission Scanning Electron Microscopy (FESEM). $La_2Fe_2O_6$ is an important member of the synthesis family, as it is a promising candidate for ultrahigh-density magnetic

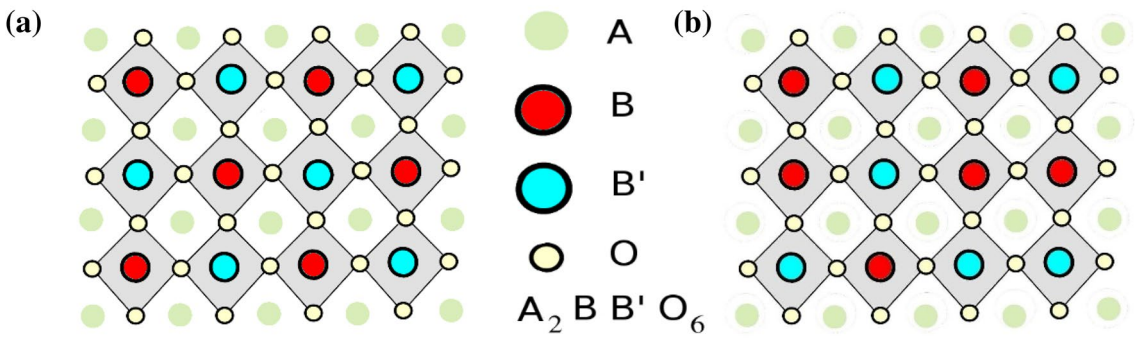

Fig. 8 Two models of double perovskite. **a** Ideal structure and **b** random antisite disorder (Singh 2012)

recording. While the usage of La_2FeNiO_6 as cores of transformers can be attributed to its narrow hysteresis loops that, limit the energy loss in form of heat. The competition between the various magnetic exchange interactions with different magnetic ASD initiatives the system to spin glass state. The exchange bias in the investigated samples gives strong evidence for the existence of the APBs in double perovskite samples. One can modulate the exchange bias effect in the investigated samples by changing B″ type (Fe, Co and Ni).

Compliance with ethical standards

Conflict of interest There is no conflict of interest.

References

Abbas YM et al (2019) Investigation of structural and magnetic properties of multiferroic $La_{1-x}Y_xFeO_3$ perovskites, prepared by citrate auto-combustion technique. J Magn Magn Mater 482:66–74

Aguilar B, Soto TE, de la TorreMedina J, Navarro O (2019) Curie temperature enhancement in the double perovskite $Sr_{2-x}La_xFeMoO_6$. Phys B Condens Matter 556:108–113

Ahmed T, Chen A, Yarotski DA, Trugman SA, Jia Q, Zhu JX (2017) Magnetic, electronic, and optical properties of double perovskite Bi_2FeMnO_6. APL Mater 5:5601. https://doi.org/10.1063/1.4964676

Alarcón-Suesca CE, Deluque Toro CE, Gil Rebaza AV, Landínez Téllez DA, Roa-Rojas J (2019) Ab-initio studies of electronic, structural and thermophysical properties of the Sr_2TiMoO_6 double perovskite. J Alloys Compd 771:1080–1089

Almessiere MA, Slimani Y, Baykal A, Trukhanov SV, Trukhanov AV (2019) Manganese/yttrium codoped strontium nanohexaferrites: evaluation of magnetic susceptibility and mossbauer spectra. Nanomaterials 9:1–18. https://doi.org/10.3390/nano9010024

Anderson MT, Greenwood KB, Taylor GA, Poeppelmeier KR (1993) B-cation arrangements in double perovskites. Prog Solid State Chem 22(3):197–233

Asaka T et al (2007) Strong pinning effect and magnetic nanodomain formation by coupling between magnetic and crystallographic domains in the ordered double perovskite Ba_2FeMoO_6. Phys Rev B 75:1–6

Ateia EE, Mohamed AT (2017) Improvement of the magnetic properties of magnesium nanoferrites via CO^{2+}/Ca^{2+} doping. J Supercond Nov Magn 30:627–633

Ateia E, Abdelamksoud MK, Rizk MA (2017) Improvement of the physical properties of novel (1–x) $CoFe_2O_4$ + (x) $LaFeO_3$ nanocomposites for technological applications. J Mater Sci Mater Electron 28:16547–16553

Ateia EE, Mohamed AT, Morsy M (2019) Humidity sensor applications based on mesopores LaCoO3. J Mater Sci Mater Electron 30:19254–19261. https://doi.org/10.1007/s10854-019-02284-y

Ateia EE, Ramadan R, Shafaay AS (2020a) Efficient treatment of lead-containing wastewater by $CoFe_2O_4$/graphene nanocomposites. Appl Phys A 126(1):8

Ateia EE, Abdelmaksoud MK, Arman MM et al (2020b) Comparative study on the physical properties of rare-earth-substituted nano-sized $CoFe_2O_4$. Appl Phys A 126(2):1–10. https://doi.org/10.1007/s00339-020-3282-5

Bhagwat M, Ramaswamy AV, Tyagi AK, Ramaswamy V (2003) Rietveld refinement study of nanocrystalline copper doped zirconia. Mater Res Bull 38:1713–1724

Dhilip M, Devi NA, Punitha JS, Anbarasu V, Kumar KS (2019) Conventional synthesis and characterization of cubically ordered La_2FeMnO_6 double perovskite compound. Vacuum 167:16–20

Erten O, Meetei ON, Mukherjee A, Randeria M, Trivedi N, Woodward P (2011) Theory of half-metallic ferrimagnetism in double perovskites. Phys Rev Lett 107(257201):1–4

Fuster V, Druker AV, Baruj A, Malarría J, Bolmaro R (2015) Characterization of phases in an Fe–Mn–Si–Cr–Ni shape memory alloy processed by different thermomechanical methods. Mater Charact 109:128–137

Ghaffari M, Shannon M, Hui H, Kiang O, Irannejad A (2012) Preparation, surface state and band structure studies of $SrTi_{(1-x)}Fe_{(x)}O_{(3-\delta)}$ (x = 0–1) perovskite-type nano structure by X-ray and ultraviolet photoelectron spectroscopy. Surf Sci 606(5–6):670–677

Gorodea IA (2014) Influence of the B-site cation nature on crystal structure and magnetic properties of Ca_2BMoO_6 (B = Cr, La, Sm) double perovskite. Acta Chem Iasi 154:145–154

Harbi A et al (2019) The effect of cation disorder on magnetic properties of new double perovskites $La_2Ni_xCo_{1-x}MnO_6$ (x = 0.2–0.8). J Alloys Compd 778:105–114

Jin C (2017) Synthesis and nonlinear optical property of polycrystalline. Appl Phys A 123(4):1–5

Jørgensen CK, Berthou H (1972) Split photo-electron-signals from the unique closed-shell cation lanthanum (III). Chem Phys Lett 13(3):1–4

Joshi S, Kamble VB, Kumar M, Umarji AM, Srivastava G (2016) Nickel substitution induced effects on gas sensing properties of cobalt ferrite nanoparticles. J Alloys Compd 654:460–466

Ke S, Fan H, Huang H (2009) Dielectric relaxation in A_2FeNbO_6 (A = Ba, Sr, and Ca) perovskite ceramics. J Electroceram 6:252–256

Kimura T, Sawada H, Terakura K (1998) Room-temperature magneto resistance in an oxide material with an ordered double-perovskite structure. Nature 395:677–680

Krishna Murthy J, Jyotsna G, Nileena N, Anil Kumar PS (2017) Strain induced ferromagnetism and large magnetoresistance of epitaxial $La_{1.5}Sr_{0.5}CoMnO_6$ thin films. J Appl Phys 122:065307

Li Q et al (2014) The effect of Ca-substitution in La-site on the magnetic properties of La_2CoMnO_6. J Appl Phys 116:3–7

Lira-Hernández IA, Barrientos-Hernández FR, Pérez-Labra M, García-Mercado AM, Romero-Serrano JA (2016) Comments about Rietveld analysis and tolerance factor: Y doped $BaTiO_3$. Preprints. https://doi.org/10.20944/preprints201610.0126.v1

Manik SK, Pradhan SK (2004) Microstructure characterization of ball milled prepared nanocrystalline perovskite $CaTiO_3$ by Rietveld method. Mater Chem Phys 86:284–292

Markandeya Y, Reddy YS, Bale S (2015) Characterization and thermal expansion of $Sr_2Fe_xMo_{2-x}O_6$ double perovskites. Bull Mater Sci 38(6):1603–1608

Morrow R, Freeland JW, Woodward PM (2014) Probing the Links between Structure and Magnetism in $Sr_{2-x}Ca_xFeOsO_6$ double perovskites. Inorg Chem 53:7983–7992

Mumtaz A, Khan M, Janjua BH, Hasanain K (2007) Exchange bias and vertical shift in $CoFe_2O_4$ nanoparticles. J Magn Magn Mater 313:266–272

Navarro J, Balcells L, Sandiumenge F, Roig A, Martinez B, Fontcuberta J (2001) Antisite defects and magnetoresistance in Sr_2FeMoO_6 double perovskite. J Phys C Condens Matter 13:8481

Pilania G, Uberuaga BP, Ramprasad R, Gubernatis JE (2016) Machine learning bandgaps of double perovskites. Sci Rep 6:1–10

Rajagopalan R, Chen B (2017) Improved reversibility of Fe^{3+}/Fe^{4+} redox couple in sodium super ion conductor type $Na_3Fe_2(PO_4)_3$ for sodium-ion batteries. Adv Mater 29(12):1605694

Sahoo RC, Giri SK, Paladhi D, Das A, Nath TK (2016) Evidence of cluster-glass-like state at low temperature in anti-site disordered $La_{1.5}Ca_{0.5}CoMnO_6$ double perovskite. J Appl Phys 120:033906. https://doi.org/10.1063/1.4958980

Sclauzero G, Dymkowski K, Ederer C (2016) Tuning the metal-insulator transition in d^1 and d^2 perovskites by epitaxial strain: a first principles-based study. Phys Rev B 94:1–11

SilvaRX, Reichlova H, Marti X, Paniago R, Paschoal CWA (2018) Anti-ferromagnetic interaction in double perovskites probed by Raman spectroscopy.

Singh VN (2012) The impact of antisite disorder on magnetism and transport in the double perovskites. A Thesis submitted to the Board of Studies in Physical Science Discipline, Homi Bhabha National Institute. http://hdl.handle.net/10603/11360

Singh J, Kumar A (2019) Facile wet chemical synthesis and electrochemical behavior of La_2FeCoO_6 nano-crystallites. Mater Sci Semicond Process 99:8–13

Singh VN, Majumdar P (2011) Antisite domains in double perovskite ferromagnets: impact on magnetotransport and half-metallicity. EPL 94:1–6. https://doi.org/10.1209/0295-5075/94/47004

Sudha, Saxena M, Balani K, Maiti T (2019) Structure and thermoelectric properties of calcium doped Sr_2TiCoO_6 double perovskites. Mater Sci Eng B 244:65–71

Tezuka K, Henmi K, Hinatsu Y, Masaki NM (2000) Magnetic susceptibilities and Mossbauer spectra of perovskites A_2FeNbO_6 (A = Sr, Ba). J Solid State Chem 154:591–597

Tulliani J, Maria M, Tortora L, Sora IN (2015) Ageing of lanthanum strontium copper orthoferrite powders for sensing layers. Chem Eng Trans 43(2013):1807–1812

Uhlenbrockt S, Scharfschwerdtt C, Neumannt M, Illing G, Freund H-J (1992) The influence of defects on the Ni 2p and 0 1s XPS of NiO. J Phys Condens Matter 4:7973–7978

Vandana CS, Rudramadevi BH (2017) Rietveld study of Cu doped gadolinium orthoferrites. IJRASET 5:1999–2004

Vasala S, Karppinen M (2015) $A_2B_0B_{00}O_6$ perovskites: a review. Prog Solid State Chem 43:1–36

Xu X, Zhong Y, Shao Z (2019) Double perovskites in catalysis, electrocatalysis, and photo(electro)catalysis. Trends Chem 1–15

Zhao K et al (2016) Preparation of double perovskite-type oxide $LaSrFeCoO_6$ for chemical looping steam methane reforming to produce syngas and hydrogen. J Rare Earths 34(10):1032–1041

Publisher's Note Springer Nature remains neutral with regard to jurisdictional claims in published maps and institutional affiliations.